Acta Biomaterialia 9 (2013) 7014–7024

Contents lists available at SciVerse ScienceDirect

Acta Biomaterialia

journal homepage: www.elsevier.com/locate/actabiomat

Unique microstructural design of ceramic scaffolds for bone regeneration under load

S.I. Roohani-Esfahani [a], C.R. Dunstan [a], J.J. Li [a], Zufu Lu [a], B. Davies [a], S. Pearce [b], J. Field [c], R. Williams [d], H. Zreiqat [a,*]

[a] Biomaterials and Tissue Engineering Research Unit, School of AMME, The University of Sydney, Sydney 2006, Australia
[b] University of Ballarat B, Victoria 3350, Australia
[c] Flinders University, Adelaide 5001, Australia
[d] Adelaide Microscopy, The University of Adelaide, South Australia 5005, Australia

ARTICLE INFO

Article history:
Received 3 September 2012
Received in revised form 23 January 2013
Accepted 22 February 2013
Available online 1 March 2013

Keywords:
Bone regeneration
Scaffold
Osteoconduction
In vivo test
In vitro test

ABSTRACT

During the past two decades, research on ceramic scaffolds for bone regeneration has progressed rapidly; however, currently available porous scaffolds remain unsuitable for load-bearing applications. The key to success is to apply microstructural design strategies to develop ceramic scaffolds with mechanical properties approaching those of bone. Here we report on the development of a unique microstructurally designed ceramic scaffold, strontium–hardystonite–gahnite (Sr–HT–gahnite), with 85% porosity, 500 μm pore size, a competitive compressive strength of 4.1 ± 0.3 MPa and a compressive modulus of 170 ± 20 MPa. The in vitro biocompatibility of the scaffolds was studied using primary human bone-derived cells. The ability of Sr–HT–gahnite scaffolds to repair critical-sized bone defects was also investigated in a rabbit radius under normal load, with β-tricalcium phosphate/hydroxyapatite scaffolds used in the control group. Studies with primary human osteoblast cultures confirmed the bioactivity of these scaffolds, and regeneration of rabbit radial critical defects demonstrated that this material induces new bone defect bridging, with clear evidence of regeneration of original radial architecture and bone marrow environment.

1. Introduction

The gold standard for bone defect repair – bone grafting with autologous bone – has significant drawbacks, such as limited availability, second site surgery and donor site morbidity, leading to prolonged hospitalization [1]. Allografting also has several disadvantages which limit its use, including reduced bioactivity and increased risk of disease transmission. Consequently, the search for an alternative bone graft substitute that reproduces bone's structural properties combined with the necessary porosity, interconnectivity, bioactivity and mechanical strength is one of the key challenges facing scientists in the field [2,3]. A critical limitation in almost any biomaterial approach to the repair and regeneration of large bone defects in load-bearing applications is the balance between material properties, implant architecture and bioactivity to satisfy requirements for strength and toughness, as well as osteoconductivity and osteoinductivity. During the past 30 years, a variety of synthetic bone graft substitutes based on ceramics and glasses have become available, composed of materials such as bioactive glasses (modified and unmodified, beta-tricalcium phosphate (β-TCP), hydroxyapatite (HA) and TCP/HA). While they have excellent properties for bone regeneration and bioactivity, their mechanical properties are inadequate for load-bearing applications in the highly porous form (porosity >80%, pore size >300 μm and 100% interconnectivity between the pores) necessary for vascularization and bone ingrowth [4–8]. The composition and degradation of bioactive glasses are easily controlled, making them attractive scaffolds for use in bone regeneration. However, their lack of microstructure and long-range order contributes to their very low resistance to crack propagation and an extreme sensitivity to flaws, leading to catastrophic failure of the scaffolds under load [5,9–12]. Ceramics, on the other hand, exhibit ordered structures with micromorphological features (i.e. grains) that promote increased toughness compared to glasses. The fracture toughness (K_{1C}) for glass materials is inherently low (K_{1C} = 0.5–1) compared to crystalline ceramic materials, with typical K_{1C} values ranging from 0.5 to 5 (and from 6 to 15 for stabilized zirconia) [5,11,12]. However, ceramic scaffolds are inherently brittle, and are fabricated by sintering low-efficiency-packed powders, which is a contributing factor to their low strength [13–15]. This leads to the formation of a poorly sintered and weak scaffold. During the

* Corresponding author. Tel.: +61 293512392; fax: +61 2 9351 7060.
E-mail address: hala.zreiqat@sydney.edu.au (H. Zreiqat).

1742-7061/$ - see front matter © 2013 Acta Materialia Inc. Published by Elsevier Ltd. All rights reserved.
http://dx.doi.org/10.1016/j.actbio.2013.02.039

past two decades, much effort has been directed towards improving the toughness and strength of dense ceramics, in order to prevent crack growth and formation of flaws [5,10,16–18]. The unsolved problem is that toughness is usually inversely proportional to strength, such that the design of a strong and tough ceramic material is inevitably compromised [10]. We believe that the key for producing a ceramic scaffold with optimal strength and toughness lies in the application of microstructural design strategies which can promote crack-tip shielding mechanisms, such as crack deflection and, most importantly, crack bridging [19]. The other main issue with current materials is their limited innate bioactivity relative to autologous bone grafts. Attempts to address this have included the addition of biologics such as bone morphogenetic protein or mesenchymal stem cells to enhance their bioactivity, both strategies substantially increasing the cost and complexity of their clinical development and use [20–22].

In the present study, we introduce a new ceramic with a devised microstructural design produced with the aim of developing a mechanically strong and tough material for use in highly porous scaffolds. We incorporated Ca, Sr, Zn and Si ions in this material with the added aim of enhancing its bioactivity [23,24]. In this study we assessed the mechanical properties of this scaffold and evaluated its in vitro and in vivo bioactivity.

2. Materials and method

2.1. Preparation of solid and porous ceramics

Sr–$Ca_2ZnSi_2O_7$ powders were prepared by the sol–gel process using tetraethyl orthosilicate ($(C_2H_5O)_4Si$, TEOS), zinc nitrate hexahydrate ($Zn(NO_3)_2{\cdot}6H_2O$), calcium nitrate tetrahydrate ($Ca(NO_3)_2{\cdot}4H_2O$) and strontium nitrate ($Sr(NO_3)_2$) as raw materials (all from Sigma–Aldrich, USA). The TEOS was mixed with water and 2 M HNO_3 (mol ratio: $TEOS/H_2O/HNO_3 = 1:8:0.16$) and hydrolyzed for 30 min under stirring. Then, the $Zn(NO_3)_2{\cdot}6H_2O$, $Ca(NO_3)_2{\cdot}4H_2O$ and $Sr(NO_3)_2$ (5 wt.%) solutions were added into the mixture (mol ratio: $TEOS/Zn(NO_3)_2{\cdot}6H_2O/Ca(NO_3)_2{\cdot}4H_2O = 2:1:2$), and reactants were stirred for 5 h at room temperature. After the reaction, the solution was maintained at 60 °C for 1 day and dried at 120 °C for 2 days to obtain the dry gel. The dry gel was calcined at 1200 °C for 3 h. The resulting powders consisted mainly of Ca (25.55 wt.%), Si (17.90 wt.%) and O (35.69 wt.%). The ternary phase diagram of the Al_2O_3–CaO–SiO_2 system displays a number of invariant compositions with low melting points. The lowest is 1170 °C for the eutectic composition of 62.0% SiO_2, 23.3% CaO and 14.7% Al_2O_3. In order to provide a glass phase at the grain boundaries by forming a liquid phase during sintering, an optimum amount of aluminum oxide powder (15 wt.%) was added to the Sr–$Ca_2ZnSi_2O_7$ powder, and the powders were mixed and ground by a ball mill machine before preparation the scaffolds and disks for 2 h at 150 rpm. TCP/HA powder and scaffolds were prepared based on previous published work [25]. A polymer sponge replication technique was used for fabrication of Sr–HT–gahnite scaffolds according to a previous report [25]. For preparing the Sr–HT–gahnite disk samples, the powders were pressed by a steel die and sintered at 1250 °C for 3 h.

2.2. Physical and chemical properties of the scaffolds

The microstructure and fracture surface of the scaffolds and disks were evaluated by field emission scanning electron microscopy (FE-SEM; Carl Zeiss, Germany). Three-dimensional architecture of porous scaffolds was assessed by micro-computed tomography (μCT; SkyScan 1072, Belgium) (reconstructed images not shown). Chemical composition of the prepared scaffolds was analyzed by elemental analysis and mapping (EDS) and X-ray diffraction (XRD).

2.3. Degradation of scaffolds in simulated body fluid

In vitro biodegradation of the scaffolds was investigated by soaking the scaffolds in simulated body fluid (SBF). The SBF solution was prepared according to the procedure described by Kokubo and Takadama [26]. Cubic scaffolds ($8 \times 8 \times 8$ mm) were immersed in SBF solution at 37 °C for 1, 7, 14, 21 and 28 days at a solid/liquid ratio of 150 mg l^{-1}. All scaffolds were held in plastic flasks and sealed. At each time point the scaffolds were removed, rinsed with Milli-Q water and dried at 100 °C for 2 days, after which the final weight of each scaffold was measured. The concentration of ions in the SBF after soaking the scaffolds was tested using inductive coupled plasma atomic emission spectroscopy (ICP-AES; Perkin Elmer, Optima 3000DV, USA). The weight loss was calculated as a percentage of the initial scaffold weight. Three scaffolds from each sample group were used to measure the weight loss and pH changes and the results are expressed as means ± SD.

2.4. Mechanical properties of the scaffolds

Mechanical properties of the scaffolds were determined in both dry and wet conditions on five identical specimens from each sample group. For wet conditions, the scaffolds were first soaked in SBF for different time periods and excess liquid was carefully removed with filter paper prior to testing. Compressive strength was determined by crushing cubic scaffolds (7 mm × 7 mm × 7 mm) between two flat plates using a computer-controlled universal testing machine (Instron 8874, UK) with a ramp rate of 0.5 mm min^{-1}. Compressive strength and modulus of solid samples were determined according to ASTM C1424. Toughness value (amount of the energy per volume that a material can absorb before fracture (in unit of J m^{-3})) was determined by integrating the area under the stress–strain curve from zero to the point of maximum stress [27]. Vickers hardness values were calculated by use of the ASTM C1327. Fracture toughness was measured using two methods; the Anstis [28] and the single-edge notched beam (SENB) methods [29–31]. For the Anstis method, a radial crack from the corners of indentation was induced on the polished surface of the ceramics ($n = 10$). The crack lengths were measured in order to calculate the toughness value according to the following equation:

$$K_c = 0.16\left(\frac{E}{H}\right)^{1/2}\left(\frac{\rho}{C_0^{3/2}}\right) \quad (1)$$

H is the measured hardness using an applied load (ρ) of 9.8 N. Measurement of crack length (C_0) was achieved by creating reproducible radial cracks by applying a load of 98 N. E is the compressive modulus which was derived from the linear region of the stress–strain curve of solid samples. Fracture toughness was evaluated by the SENB method with a 31 mm span and cross-head speed of 0.05 mm min^{-1} using 3 mm × 4 mm × 40 mm test bars on a jig used for three-point bending tests. Each specimen was ground and polished down to 1 μm finish and its sharp edges were chamfered. The notches of the specimen were cut with a 0.2 mm diamond. The saw depth was nearly half of the specimen's height.

2.5. In vitro evaluation by cell culture

2.5.1. Scaffold sterilization

Cubic scaffolds with dimensions of 5 mm × 5 mm × 5 mm were sterilized by soaking twice in 70% ethanol for 30 min each time, followed by rinsing three times with phosphate-buffered saline

(PBS) for 15 min each time, after which the scaffolds were exposed to UV light for 30 min.

2.5.2. Human osteoblast cell isolation, seeding and culture

Permission to use discarded human tissue was granted by the Human Ethics Committee of the University of Sydney and informed consent was obtained. An established method for culturing osteoblast cells was used as previously described. Human osteoblast cells (HOBs) were isolated from normal human trabecular bone. The bone was divided into 1 mm^3 pieces, washed several times in PBS and digested for 90 min at 37 °C with 0.02% (w/v) trypsin (Sigma–Aldrich, USA) in PBS. Digested cells were cultured in complete medium containing α-minimal essential medium (α-MEM) (Gibco Laboratories, USA), supplemented with 10% (v/v) heat-inactivated fetal calf serum (FCS) (Gibco Laboratories, USA), 2 mM l-glutamine (Gibco Laboratories, USA), 25 mM Hepes buffer (Gibco Laboratories, USA), 2 mM sodium pyruvate, 100 U ml^{-1} penicillin, 100 μg ml^{-1} streptomycin (Gibco Laboratories, USA) and 1 mM l-ascorbic acid phosphate magnesium salt (Wako Pure Chemicals, Japan). The cells were cultured at 37 °C with 5% CO_2 and complete medium changes were performed every 3 days. All HOBs used in the experiments were at passage 3. After the cells reached 80–90% confluence, they were trypsinized with TrypLE™ Express (Invitrogen, USA) and subsequently suspended in complete medium. For HOB attachment and proliferation studies, cells were seeded on the scaffolds at initial cell densities of 1.5×10^5 cells per scaffold and 5×10^4 cells per scaffold, respectively, in 90 μl of cell suspension. For the gene expression study, cells were seeded on the scaffolds at an initial cell density of 2×10^5 cells per scaffold in 100 μl of cell suspension. The seeding suspension of HOBs was gently dropped onto each scaffold ($n = 4$), placed in 24-well plates (untreated, NUNC) and incubated for 90 min at 37 °C to allow cell attachment. Each scaffold was then transferred to a new well and 1.5 ml of culture medium was added. At designated time points, HOBs on the scaffolds were analyzed for attachment, viability and gene expression. If HOBs were observed to have migrated from the scaffold and grown on the well, the scaffold was transferred to a new well for examinations.

2.5.3. HOB attachment, proliferation and differentiation

HOB attachment was evaluated after 2 and 24 h of culture. At each time point, scaffolds were prepared for SEM examination. Scaffolds with cells were fixed with 4% paraformaldehyde solution, post-fixed with 1% osmium tetroxide in PBS for 1 h, dehydrated in graded ethanol (30%, 50%, 70%, 95% and 100%), dried in hexamethyldisilizane for 3 min and then desiccated overnight. The scaffolds were gold sputtered prior to SEM examination. To evaluate HOB proliferation, the CellTiter 96 Aqueous Assay (Promega, USA) was used to determine the number of viable cells on the cultured scaffolds via a colorimetric method. The assay solution is a combination of tetrazolium compound (3-(4,5-dimethylthiazol-2-yl)-5-(3-carboxymethoxyphenyl)-2-(4-sulfophenyl-2H-tetrazolium), MTS) with an electron coupling reagent (phenazine methosulfate) at a volume ratio of 20:1. The former compound can be bioreduced by viable cells into formazan, which is soluble in cell culture medium, and the absorbance of formazan at 490 nm is directly proportional to the number of viable cells present. HOB proliferation was evaluated after 1 and 7 days of culture. At each time point, the culture medium was replaced by 1.5 ml of the MTS working solution, which consisted of the CellTiter 96 Aqueous Assay solution diluted in PBS at a volume ratio of 1:5. After 4 h of incubation at 37 °C, 100 μl of the working solution was transferred to a 96-well cell culture plate, and the absorbance at 490 nm was recorded using a microplate reader (PathTech, Australia) using the software Accent. Total RNA was isolated from HOBs by adding Trizol reagent (Invitrogen, USA) after removing the culture medium, according to the manufacturer's instructions. First-strand cDNA was synthesized from 0.7 μg total RNA using the Omniscript RT Kit (Qiagen, USA) according to the manufacturer's instructions. Real-time PCR was performed using Rotor-Gene 6000 (Corbett Life Science, USA) by using Immomix (Bioline, UK) according to the manufacturer's instructions. The relative gene expression levels for Runx2, collagen type I, bone sialoprotein and osteocalcin were obtained by normalizing them to a housekeeping gene (18S). Primers for the selected genes have been previously described.

2.6. Evaluation of the Sr–HT–gahnite scaffold in a radial segmental defect in rabbits

The in vivo effectiveness of Sr–HT–gahnite compared to the clinically relevant TCP/HA was assessed by implantation of porous scaffolds into segmental defects in the radius of rabbits [32]. As the ulna provided significant mechanical support in this model, internal fixation was not required. However, partial load was transmitted to the scaffold through weight bearing and muscle activity. We prepared highly porous and interconnected scaffolds composed of Sr–HT–gahnite and the clinically used TCP/HA as a control material. A total of 12 male rabbits (New Zealand White, 20 weeks of age) were used for in vivo evaluation. This model is considered by convention to be a critical-sized defect, although there is some dispute in the literature as 15 mm defects have been shown to regenerate to some extent over a 12 week period [33]. Nonetheless, this model is well described and appropriate for evaluating selected biomaterials to predict their performance in an orthopedic load-bearing environment. The animal experiment was performed according to a protocol reviewed and approved by the Flinders University Animal Welfare Committee. The rabbit model was unilateral, and a consistent location for ostectomy in each animal was achieved by ensuring that the ostectomy was positioned immediately proximal to the fibrous insertion of the pronator teres. The rabbits received 0.4 mg kg^{-1} diazepam subcutaneously 15 min prior to mask induction with isoflurane 4% in 100% oxygen, delivered by a T-piece circuit with a fresh gas flow rate of 3.5 l min^{-1}. Upon induction of stable anesthesia, 2.5% isoflurane was delivered at the same fresh gas flow rate. The rabbit was placed in lateral recumbency with the operated limb dependent. The limb was prepared for aseptic surgery and draped to isolate the surgical site. A 2.5 cm surgical incision was made over the dorso-medial aspect of the forearm, and the underlying tissues separated to reveal the radial bone. Two parallel cuts were made 15 mm apart, and the excised radial bone was removed from the defect. The ulna was left intact. Animals were randomized to implantation with either Sr–HT–gahnite or TCP/HA. The implant (4 mm × 4 mm × 15 mm) was placed into the defect, and the wound closed in three layers using an absorbable suture material (3–0 vicryl). One scaffold of TCP/HA ($n = 6$) or Sr–HT–gahnite ($n = 6$) was implanted in each rabbit. Following placement of the implant, the wound was closed. The rabbits were recovered and maintained for 12 weeks with ample space for exercise to allow normal weight bearing of the implanted limb. Perioperative antimicrobial therapy was provided in the form of cephalosporin at 30 mg kg^{-1} by intramuscular injection. Analgesia was provided by the administration of meloxicam at 0.2 mg kg^{-1} by intramuscular injection prior to surgery, followed by every 24 h for 3 days (4 doses altogether). The post-operative explantation period for all groups was 12 weeks. Radiographs were obtained using a Kodak CR-500 digital acquisition system. Images obtained were saved as DICOM (Digital Imaging and Communications in Medicine) files. These radiographs provided qualitative and semi-quantitative measurements of defect healing, as evidenced by new bone formation and/or defect fusion.

Table 1
Scoring criteria for the radiologic evaluation of defect bridging 12 weeks after scaffold implantation.

Criteria	Score
No obvious bone regeneration	0
Less than 50% bone regeneration	1
More than 50% bone regeneration	2
Almost fused	3
Fused-not full thickness	4
Fused-full thickness	5

12 weeks after surgery, the animals were sacrificed by an intravenous overdose injection of pentobarbital. The radii and tibiae were explanted en bloc for embedding in plastic for undecalcified histology to facilitate qualitative and quantitative analysis of new bone formation in the defect.

2.6.1. New bone ingrowth and resorbability

New bone ingrowth was assessed radiographically and histologically. Radiographs were scored by two observers blinded to the scaffold material using a semi-quantitative scoring system outlined in Table 1.

2.6.2. Histological assessment and scaffold resorption

Specimens were dehydrated through graded ethanol, cleared in xylene at room temperature and then infiltrated with, and embedded in, polymethyl-methacrylate resin using a standard processing infiltration schedule as previously described [34]. Upon polymerization, multiple equidistant transverse sections through the defect region were prepared from the embedded resin block using a water-cooled slow-speed Buehler isomet saw (Buehler, Germany) and subsequently polished. The sections corresponding to the defect proximal and distal edges were identified and the midpoint sections selected as the section equidistant to these defect edges. A single midpoint section was used for histological analysis for each bone sample. Sections were surface stained with toluidine blue following surface etching (acid ethanol) and histomorphometry was conducted using image analysis software (OsteoMeasure, Osteometrics, Georgia). Bone ingrowth was evaluated within the defect boundaries, by measuring the bone volume and ceramic volume. Residual ceramic was clearly recognizable as dense black material in the sections and was readily differentiated from bone which was stained blue. The extent to which bone and ceramic surfaces were lined with bone cells was identified in sections following toluidine blue staining or after enzyme histochemistry for tartrate-resistant acid-phosphatase (TRAP) activity using naphthol-AS-BI phosphate (Sigma–Aldrich, USA) as a substrate and fast red violet LB salt (Sigma–Aldrich, USA) as a detection agent for the reaction product as previously described. Osteoblasts were identified on the basis of their cuboidal morphology in toluidine blue stained sections. Osteoclasts were identified based on positive staining for TRAP activity. Resorbability was assessed by comparing final ceramic volume for the different scaffolds and by noting the presence of osteoclasts and resorption lacunae.

2.7. Statistical analysis

All data have been presented as mean ± SD, and were derived from at least four independent samples. For statistical analysis, Levene's test was performed to determine the homogeneity of variance of data, and then either Tukey's HSD or Tamhane's post hoc tests were used. The PASW statistics program was employed for all statistical analyses and differences were considered as significant if $p < 0.05$. T-tests assuming equal variances and Mann–Whitney tests were performed to test for significance between TCP/HA and Sr–HT–gahnite. All data have been expressed as mean ± standard error unless otherwise stated. All statistical analyses were performed in Microsoft Excel and differences were considered as significant if $p < 0.05$.

3. Results and discussion

Fig. 1A shows the typical microstructure of crystalline ceramic scaffolds containing a clear grain boundary configuration with micro-sized cracks and pores [8,35–37]. Upon loading, cracks start growing from defects and propagate through the grain boundary (Fig. 1A, inset), resulting in catastrophic failure of the scaffold [35]. Fig. 1B shows the typical microstructure of a liquid phase sintered ceramic scaffold with amorphous phase wetting grain boundaries. Formation of a glass phase during sintering eliminates the defects, leading to improved strength. However, the toughness of this structure is compromised due to fast crack propagation through the glass phase (Fig. 1B inset) [38].

In the present study, we introduce a ceramic scaffold with a devised microstructural design (Fig. 1C) aiming to significantly improve scaffold strength on the one hand, and to activate crack deflection paths for enhancing toughness on the other hand. Strontium, a known anabolic factor for bone, is included at a low concentration as a simple strategy to enhance bioactivity [39].

Fig. 1C shows our proposed microstructure designed to yield a scaffold with concurrent improvement in strength and toughness. This proposed microstructure contains the following phases: (1) equiaxed crystalline grain structures with (2) a wetting glass phase at the grain boundaries and (3) dispersed submicron crystals with coherence interface in the glass phase. Based on this model, we hypothesized that cracks would propagate through the crystalline grains and the glassy grain boundary/dispersed crystals interface, resulting in significant enhancement of strength while retaining toughness.

Sr doped $Ca_2O_7Si_2Zn$ was prepared by sol–gel method and mixed with an optimum amount of Al_2O_3 (15 wt.%). The alumina powder mixed with Sr–HT initiates two reactions: it contributes to the formation of $ZnAl_2O_4$ by reacting with Zn and to melt formation based on the ternary phase diagram of Al_2O_3–CaO–SiO_2. The microstructure obtained with Sr–HT–gahnite consisted of equiaxed grains (Sr–$Ca_2O_7Si_2Zn$) embedded within a wetting glass phase at the grain boundaries, and contained dispersed submicron crystals ($ZnAl_2O_4$, gahnite). SEM examinations revealed that both TCP/HA and Sr–HT–gahnite scaffolds had similarly highly porous architecture (87% and 85%, respectively) and pore interconnectivity (~100%) (Fig. 1D and G), with an average pore size of 500 μm. The struts of the TCP/HA scaffold contained numerous cracks and defects, accounting for its compromised mechanical properties (Fig. 1E). An important consideration when sintering biphasic calcium phosphates is the thermal stability of the HA and β-TCP phases, particularly at high temperatures [40]. Controlling sintering time, temperature and monitoring the composition and densification become crucial in the fabrication of TCP/HA scaffolds. There has been always a tradeoff between densification and having a right HA/TCP ratio after the sintering process. Therefore the presence of the defects in the microstructure of a highly porous TCP/HA scaffolds is inevitable.

The Sr–HT–gahnite scaffold displayed a solid and continuous strut microstructure with no obvious cracks or cleavage (Fig. 1H). The microstructure of TCP/HA was characteristic of crystalline ceramic scaffolds, consisting of many defects in the grain boundaries (Fig. 1F), with some remnant open channels in the struts resulting from removal of the polymer template (Fig. 1D and E). In contrast, the Sr–HT–gahnite scaffold microstructure had crystalline grains engulfed by wetting amorphous grain boundaries,

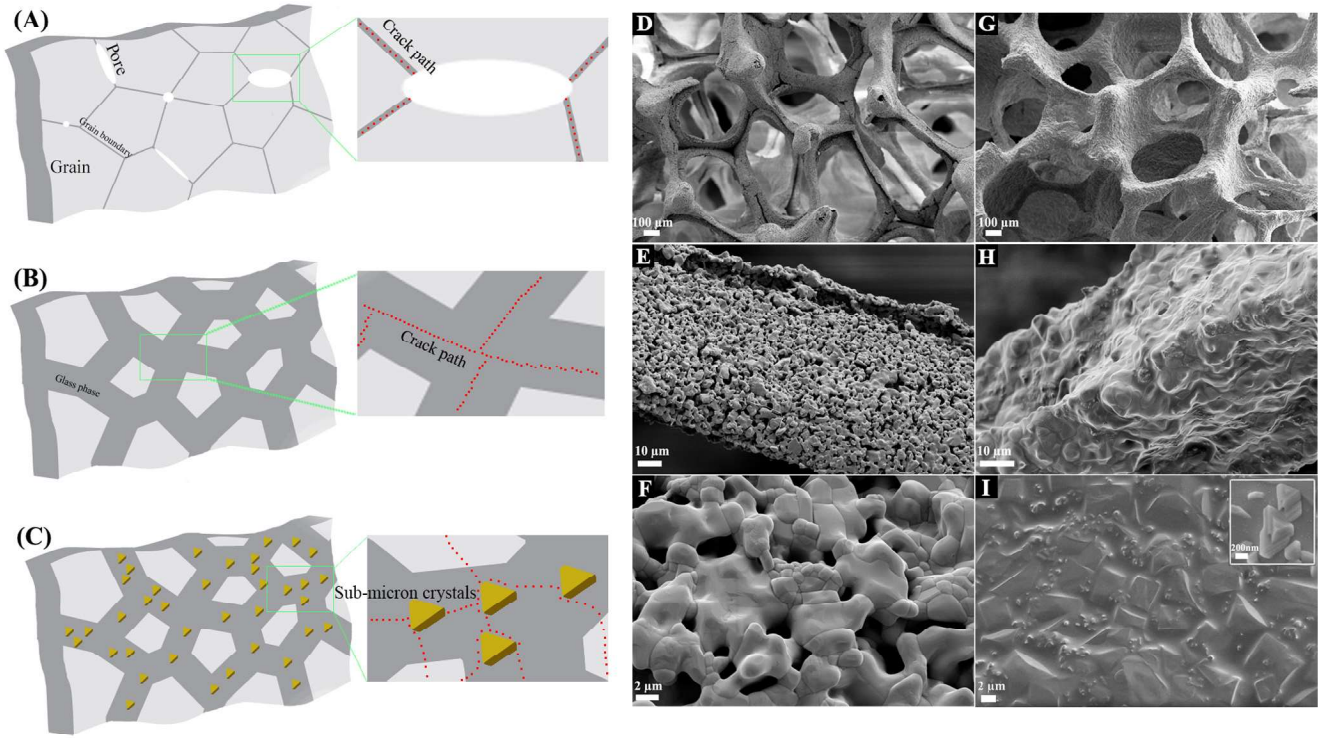

Fig. 1. Schematic diagrams of the micro- and macrostructures of the developed ceramic scaffold, compared to those which are currently available. Schematic of the microstructure of (A, B) currently available crystalline ceramic scaffolds and (C) the newly designed scaffold. (A) Type I microstructure including equiaxed grains with a clear grain boundary configuration containing microsized cracks and pores. (B) Type II microstructure, a liquid phase sintered structure containing a considerable amount of glass phase at grain boundaries. (C) The proposed microstructure contains equiaxed grains with a wetting glass phase at the grain boundaries and dispersed submicron crystals in the amorphous phase. Pore morphology and microstructure of (D–F) TCP/HA and (G–I) Sr–HT–gahnite scaffolds indicate highly porous macrostructure of both scaffolds. TCP/HA microstructure resembles type I and Sr–HT–gahnite microstructure is similar to the proposed microstructural design.

doped with dispersed submicron crystals of pyramidal shape (Fig. 1I).

The Sr–HT–gahnite ceramic is composed of two crystalline phases (Fig. 2A): Sr–$Ca_2ZnSi_2O_7$ (SrHT) (~80 wt.%) and gahnite ($ZnAl_2O_4$) (~20 wt.%). Elemental distribution analysis of strut microstructure was performed for the Sr–HT–gahnite scaffold to evaluate the qualitative distribution of Al, Zn and Si elements (Fig. 2B–D). Results showed that the dispersed crystals contained high concentrations of Al and Zn; these were confirmed as the gahnite phase by X-ray diffraction (XRD). In agreement with phase relationships at the eutectic point (1170 °C) in the ternary diagram $CaO–SiO_2–Al_2O_3$, aluminum oxide reacts with calcium and silicon in oxide form to create a melted phase. This melted phase accelerates the sintering process and mass transport to achieve a dense structure by removing the defects. The melted phase solidifies very rapidly during the cooling down step after reaching the eutectic point due to its low volume percentage. The glass phase in the grain boundaries consisted of low melting point glass oxides of Si, Al and Ca; Zn had reacted with Al during sintering forming $ZnAl_2O_4$, leaving the glass phase depleted of Zn elements.

Compressive strength and modulus of solid samples were determined according to ASTM C1424. Fracture toughness and Vickers hardness values calculated by using the Anstis method and ASTM C1327. Sr–HT–gahnite ceramic showed high compressive strength and fracture toughness (422 ± 18 MPa and 10 ± 1.5 MPa $m^{1/2}$ derived from the Anstis method and 7.4 ± 2.0 MPa $m^{1/2}$ derived from the SENB method), which are superior to cortical bone (100–150 MPa and 1.7–12 MPa $m^{1/2}$), and a compressive modulus (40 ± 7.1 GPa) close to the reported values for cortical bone (12–20 GPa); addressing the stress shielding effects encountered with the commercially available synthetic bone substitutes [7,41,42]. Compression testing of porous Sr–HT–gahnite scaffolds (85% porosity, 500 µm average pore size and 100% interconnectivity between the pores) was performed under dry and wet conditions (Fig. 2E–G). Sr–HT–gahnite scaffolds achieved a compressive strength of 4.1 ± 0.3 MPa with compressive modulus of 170 ± 20 MPa and 3.2 ± 0.1% strain at breaking point. Indeed, the compressive strength of Sr–HT gahnite scaffolds is comparable to that of cancellous bone. Fig. 2E shows the typical stress–strain curve of Sr–HT–gahnite scaffolds. The strain failure of these scaffolds was ~3%. The total area under the stress–strain curve is equivalent to the work that must be done per unit volume on the specimen before it breaks, which is an indication for toughness of the scaffold and strain energy per unit volume. This area is dramatically greater for Sr–HT–gahnite scaffolds (107 kJ m^{-3}) compared to that reported for 13–93 glass scaffolds (35 kJ m^{-3}) [43], highlighting the significant improvement in the toughness of the former. However, 13–93 glass scaffolds with an average pore size of 300 µm showed higher compressive strength and modulus with strain failure of ~0.5%. Mechanical properties of the Sr–HT–gahnite scaffold remained nearly intact (~2% degradation) after 28 days of soaking in simulated body fluid (SBF) solution (Fig. 2F), confirming only mild degradation of this material in SBF as an approximation of the biological environment. The Sr–HT–gahnite scaffold exhibited a compressive strength of 1.1 ± 0.2 MPa (Fig. 2G) when its porosity was increased to 95%, which is a competitive value when compared with the values reported for other highly porous ceramic scaffolds with even lower porosities [44,45]. Fig. 2H shows the fracture surface of Sr–HT–gahnite scaffold where the crack has been propagated through both transgranular and intergranular paths, which increases the amount of energy required for further crack propagation. Fig. 2I

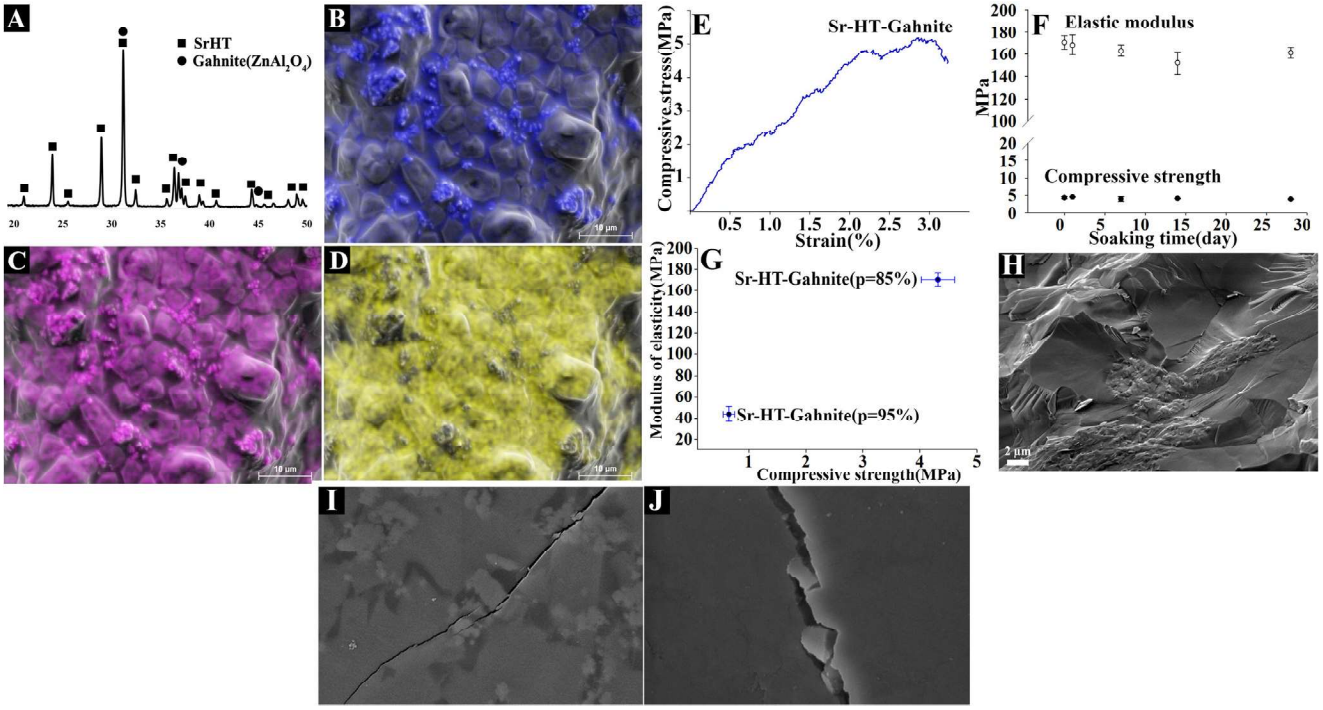

Fig. 2. Chemical, mechanical and fracture analysis of the developed scaffolds. (A–D) Chemical composition of Sr–HT–gahnite scaffolds: (A) XRD pattern and SEM images taken with secondary electron detector and EDX spectral maps of (B) Al, (C) Zn and (D) Si elements. (E) Stress–strain curves of Sr–HT–gahnite scaffold. (F) Mechanical properties of Sr–HT–gahnite scaffolds after soaking in SBF for different periods of time. (G) Compressive strength and compressive modulus of Sr–HT–gahnite scaffolds at different porosities (95% and 85%). Typical fractured struts of (H) Sr–HT–gahnite scaffolds. (I) Toughening mechanisms in Sr–HT–gahnite ceramic are indicated by microhardness testing resulting in the creation of radial cracks stemming from the microhardness indent. Closer examination (J) of the radial cracks reveals submicron crystals bridging the crack at several locations, two of which are shown in this high-resolution SEM image.

and J shows crack deflection resulting in a branched crack structure. Direct evidence of submicron-crystal pull-out and the crystals that are bridging the cracks can be observed when probing within the cracks. The fracture surface is smooth and with the appearance of steps, which form as the crack front moves from one plane to another. The formed crack in the glassy phase propagates and reaches the interface of the submicron crystals. At the interface, there are atoms which are more weakly bonded than in the bulk crystals; therefore, crack propagation assumes a wavy path and it could be an indication for improvement in toughness. Although mechanical properties of scaffolds depend primarily on the composition and microstructure of the materials, the strength of a ceramic scaffold is significantly affected by its pore size, porosity and interconnectivity. Fu et al. [46] developed a strong scaffold with a compressive strength (166 MPa) comparable to that of cortical bone. The scaffold had a large average pore size (~1.2 mm) and high interconnectivity (100%) between the pores; however, its porosity was 60%. Habibovic et al. [47] reported a compressive strength value of 6.3 MPa for HA scaffolds with 80% porosity and average pore size of 450 μm; however, the interconnectivity between the pores was drastically compromised (~50%). The nature of the fabrication process is another important factor where, for polymer sponge method, polymer removal leaves hollow struts after sintering. It means that mechanical properties can be lower than might be expected. 45S5 glass–ceramic scaffolds made by this method had a compressive strength of 0.4 MPa at 90% porosity [48]. However, Fu et al. [43] reported on fabrication of 13–93 glass scaffolds (85% porosity and 300 μm average pore size) with 11 MPa compressive strength by optimizing the processing parameters. In the case of Sr–HT–gahnite, the hollow struts fill with the melting phase, which is formed during the sintering process. Wu et al. [49] developed a glass scaffold by gel casting method and their scaffolds showed a range of compressive strength from 1.22 MPa to 2.82 MPa at different porosities from 74% to 84%.

Sol–gel-derived scaffolds have low strength (0.3–2.3 MPa), and they are suitable for substituting defects in low-load sites only [5]. Jones et al. [50] reported that it is possible to achieve a compressive strength of 2.5 MPa for a sol–gel-derived glass scaffold with 82% porosity and average pore size of 450 μm by controlling the sintering parameters. For the calcium phosphate family, particularly TCP/HA and HA scaffolds with different architectures, a range of strength, 0.01–342 MPa, has been reported where the highest values belong to pure HA [7]. Dellinger et al. [51] prepared HA scaffolds with 28% and 60% porosity with pore size range of 275 μm and 480 μm, respectively. Their scaffolds showed a compressive strength of ~300 MPa and 10 MPa. Woodward et al. [52] fabricated a HA scaffold (300 μm average pore size and 70% porosity) with 34.4 MPa compressive strength.

Considering the highly porous architecture of Sr–HT–gahnite, the measured mechanical properties of Sr–HT–gahnite scaffolds were significantly improved compared to values reported for polymer and polymer-ceramic composite scaffolds prepared by different methods [6]. Moreover, the compressive strength of Sr–HT–gahnite scaffolds was considerably higher than values reported for glass, ceramic and glass–ceramic constructs with similar porosity, pore size and interconnectivity between the pores [5–7,35,39,43–45,47,48,50,53–65] (Fig. 3A). For example, the typical compressive strength for glass–ceramic scaffolds composed of bioactive glass is 0.3–0.4 MPa, for calcium silicates is 0.32 MPa and for calcium phosphate glass is 0.8–1.4 MPa. The compressive strength of HA scaffolds in highly porous form (porosity: >80%, pore size: >300 μm) is in the range of 0.01 to 0.2 MPa [5–7,35,39,43–45,47,48,50,53–65]. Fu et al. [43] reported the highest strength reported so far for a highly porous glass scaffold (13–93), with 85%

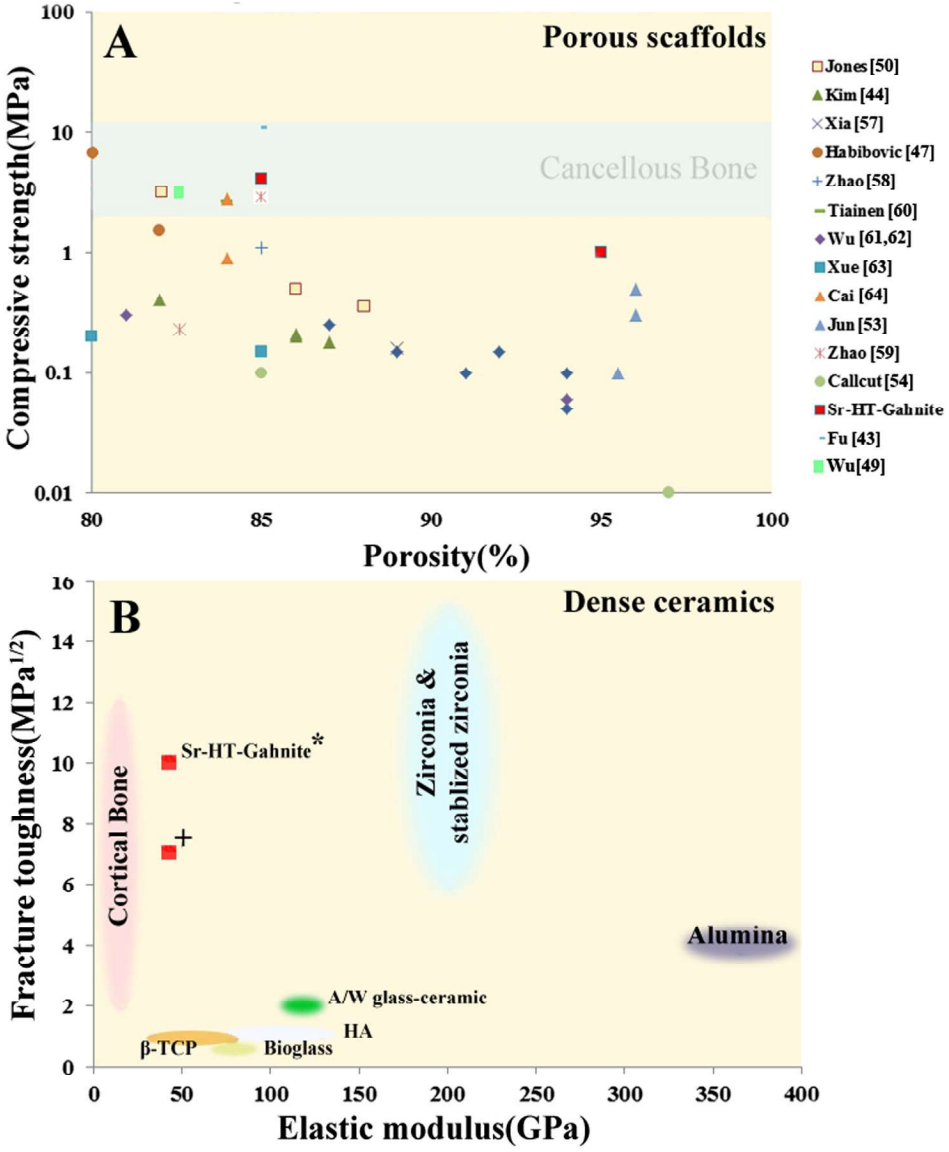

Fig. 3. (A) Compressive strength relative to porosity in highly porous ceramic, glass and glass–ceramic scaffolds ($\geqslant$80 porosity) compiled from previous studies, compared to that reported for cancellous bone and determined for Sr–HT–gahnite scaffolds. (B) Fracture toughness and elastic modulus of solid bioceramics compared to those for cortical bone and solid Sr–HT gahnite (derived from *the Anstis method and †the SENB method).

porosity and average pore size of 300 μm; however, this material would be predicted to have a low toughness due to its short range order in atomic scale, as we observed for 13–93 scaffolds. Fig. 3B compares the elastic modulus and fracture toughness of Sr–HT–gahnite with bone and with commonly used materials. It can be seen to be the only material with both toughness and elastic modulus similar to bone itself, the latter indicating reduced potential for stress shielding in loading situations. We determined the in vitro bioactivity of the Sr–HT–gahnite scaffolds using primary cultures of HOBs. HOBs cultured on Sr–HT–gahnite were more spread out and exhibited an elongated morphology (Fig. 4C and D), compared with TCP/HA (Fig. 4A and B) after 1 and 24 h of culture. The proliferation of HOBs was significantly upregulated on Sr–HT–gahnite scaffolds at 1 and 7 days compared to the TCP/HA (Fig. 4E) ($p < 0.05$). Real-time PCR results showed that the HOBs seeded on Sr–HT–gahnite scaffolds expressed significantly higher levels of collagen type I, runx2, bone sialoprotein and osteocalcin than those on TCP/HA control scaffolds at 3 and/or 7 days (Fig. 4F–I). These results suggest that osteoblasts can detect osteoinductive signals from Sr–HT–gahnite scaffolds. Critical to the assessment of Sr–HT–gahnite for use in orthopedic applications is a confirmation of in vivo biocompatibility and osteoconductivity. The superior mechanical properties of this material also provide the potential for its use in bone regeneration at load-bearing sites. For this reason, we have assessed the ability of Sr–HT–gahnite to promote bone regeneration in an orthopedically relevant model of a critical-sized defect in the radius of rabbits.

In this model, a critical-sized 1.5 cm defect was produced in the radius and filled with scaffolds composed of either Sr–HT–gahnite or the clinically relevant material TCP/HA (Fig. 5A). While much of the weight-bearing load in this model was supported by the ulna, some load was transmitted though the implant in the radius from weight bearing during ambulation and from muscle activity. Implanted Sr–HT–gahnite scaffolds (Fig. 5C) were evaluated radiographically to demonstrate extensive new bone formation with complete bridging of the radial defect at 12 weeks, compared to partial bridging observed with TCP/HA (Fig. 5B). In representative radiographs, the defect implanted with TCP/HA appears to be

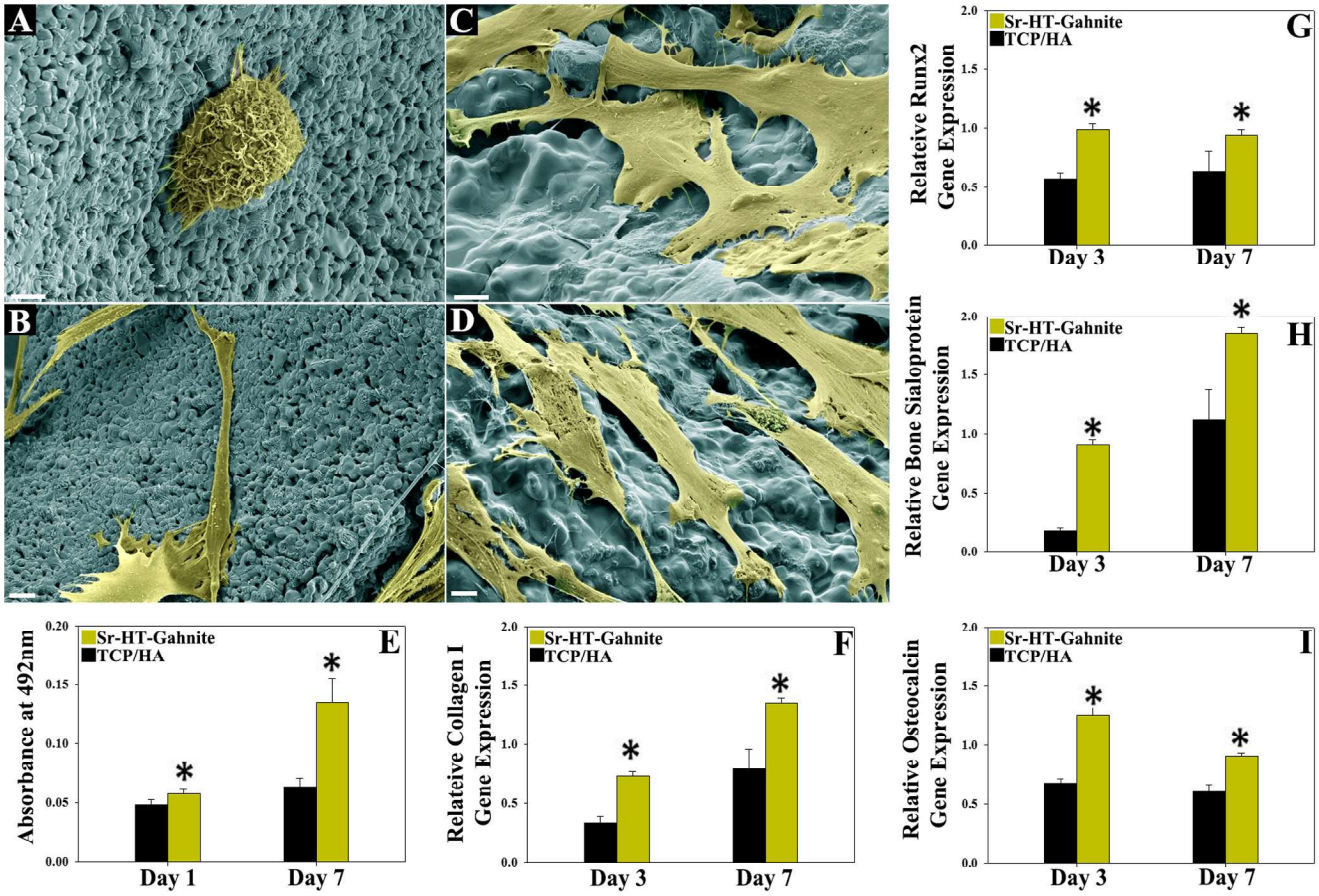

Fig. 4. Interaction of primary human bone cells (HOBs) with the scaffolds. The effects of Sr–HT–gahnite and TCP/HA scaffolds on: (A–D) attachment and spreading, (E) proliferation and (F–I) osteogenic gene expression of HOBs. HOBs cultured for (A, C) 2 h and (B, D) 24 h on (C,D) Sr–HT–gahnite was more spread out and exhibited an elongated morphology (arrows) when compared with (A, B) TCP/HA. (E) Proliferation of HOBs on Sr–HT–gahnite was significantly upregulated at day 7 compared to TCP/HA. Sr–HT gahnite also supported higher gene expression levels of (F) collagen type I, (G) Runx2, (H) bone sialoprotein and (I) osteocalcin at day 3 and/or 7. $^{*}p < 0.05$.

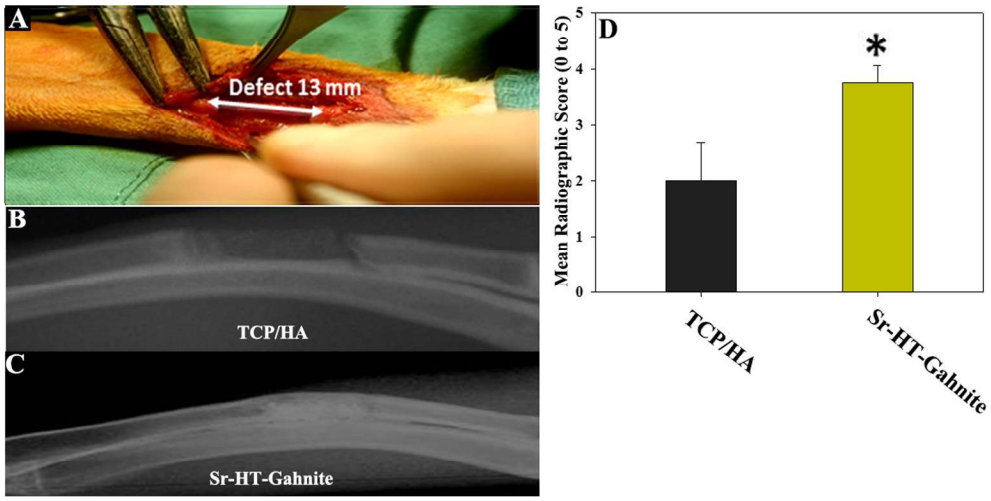

Fig. 5. Implantation of the scaffolds in an orthopedically relevant animal model and bone in growth in the defect 12 weeks after implantation. In this model, a critical-sized 13 cm defect was produced (A) in the radius and filled with either (B) TCP/HA or (C) Sr–HT–gahnite. Animals were randomized to implantation with either TCP/HA or Sr–HT–gahnite. The implant (4 mm × 4 mm × 15 mm) was placed into the defect, and the wound was closed in three layers using an absorbable suture material. (A) One scaffold of TCP/HA ($n = 6$) or Sr–HT–gahnite ($n = 6$) was implanted in each rabbit. Sections from the midpoint of the defect were used for histological analysis. (D) Blinded radiographic assessment of the repair status of defects, using a standard scoring system (0: no obvious bone regeneration, 1: less than 50% bone regeneration, 2: more than 50% bone regeneration, 3: almost fused, 4: fused – not full thickness, 5: fused – full thickness) demonstrated superior bridging of the defect for Sr–HT–gahnite scaffolds compared to the clinically relevant TCP/HA ($^{*}p < 0.05$).

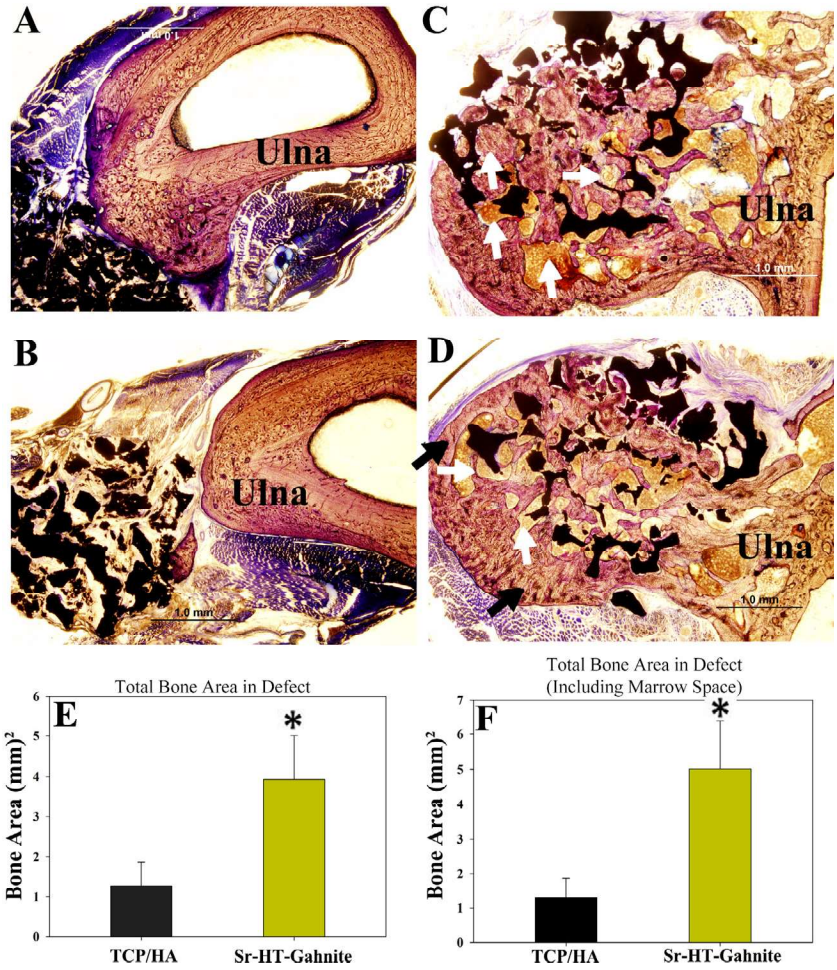

Fig. 6. In vivo bone repair in response to the scaffold implantation in a large animal model. Histological assessment of undecalcified cross-sections at the (A, C) edge and (B, D) midpoint of the defects filled with (A, B) TCP/HA or (C, D) Sr–HT–gahnite demonstrates superior new bone formation with the Sr–HT–gahnite. The presence of bone at the mid-section in the Sr–HT–gahnite scaffolds (D) demonstrates complete bridging. The preserved scaffold structure (black material) in Sr–HT–gahnite implants reflects the stronger mechanical properties of this material compared to TCP/HA, in which significant scaffold (black material) collapse can be observed. In Sr–HT–gahnite implants, more mature bone is evident at the midpoint and close to the defect edge, with re-appearance of endocortical spaces (white arrows) and formation of a cortical bone shell (black arrows). Histomorphometric assessment of total new bone formed (E) and marrow spaces (F) at the midpoint of the defects demonstrated superior bridging of the defect by the presence of significantly increased bone with the Sr–HT–gahnite ceramic ($^{*}p < 0.05$).

translucent, indicating no bridging of the defect. In contrast, the bone defect implanted with Sr–HT–gahnite is seen to contain new bone bridging the entire defect (Fig. 5C). Blinded radiographic assessment of the repair status of defects using a standard scoring system demonstrated a statistically significant improvement in defect bridging with Sr–HT–gahnite compared to the clinically relevant TCP/HA (Fig. 5D). Undecalcified histological assessment was conducted to assess the bridging of radial defects with bone when implanted with either TCP/HA or Sr–HT–gahnite. Transverse sections were taken within the defect spanning across the edge (Fig. 6A and C) of the defect and through its midpoint (Fig. 6B and D). Toluidine blue staining revealed that Sr–HT–gahnite scaffolds were well tolerated by host tissue with no signs of rejection, necrosis or infection. At 12 weeks post-implantation, extensive new bone formation was evident both at the periphery and in close proximity to the ceramics within the pores of all Sr–HT–gahnite scaffolds tested. Bone also filled in the pores within the plane of cortical bone for all scaffolds (Fig. 6C and D). In contrast, the repair response to TCP/HA scaffolds differed from Sr–HT–gahnite. Although well tolerated, the structural integrity of TCP/HA scaffold implants was lost with evidence of scaffold compaction. Also, bone tended to grow between the scaffold and ulna adjacent to the implant edge rather than through the ceramic pores (Fig. 6A and B).

Defects implanted with Sr–HT–gahnite demonstrated extensive new bone formation at both the defect edge (Fig. 6C) and at the midpoint (Fig. 6D), indicating complete defect bridging. In contrast, little new bone formation was observed for defects implanted with TCP/HA (Fig. 6A and B), particularly at the defect midpoint (Fig. 6B). In addition, scaffold architecture was much better preserved for Sr–HT–gahnite, which is consistent with its superior mechanical properties (Fig. 6C and D). The appearance of marrow spaces (indicated by white arrows in Fig. 6C and D) within the bone, formed in response to the Sr–HT–gahnite scaffolds, indicates that bone remodeling is occurring and that normal cortical architecture is being regenerated. This also suggests that a normal endocortical environment suitable for bone marrow regeneration is present (Fig. 6C and D). These effects were more prominent close to the edge (Fig. 6C) of the defect than at the midpoint (Fig. 6D), presumably because the edge represents a region where new bone formation is at a more mature stage than the midpoint.

Histomorphometric assessment of total new bone formed excluding (Fig. 6E) or including marrow spaces (Fig. 6F) at the midpoint of the defects confirmed a significantly increased area of new bone in the Sr–HT–gahnite treated defects compared to TCP/HA, consistent with complete defect bridging. Ceramic area was also measured in the histological sections at the midpoint of the defect

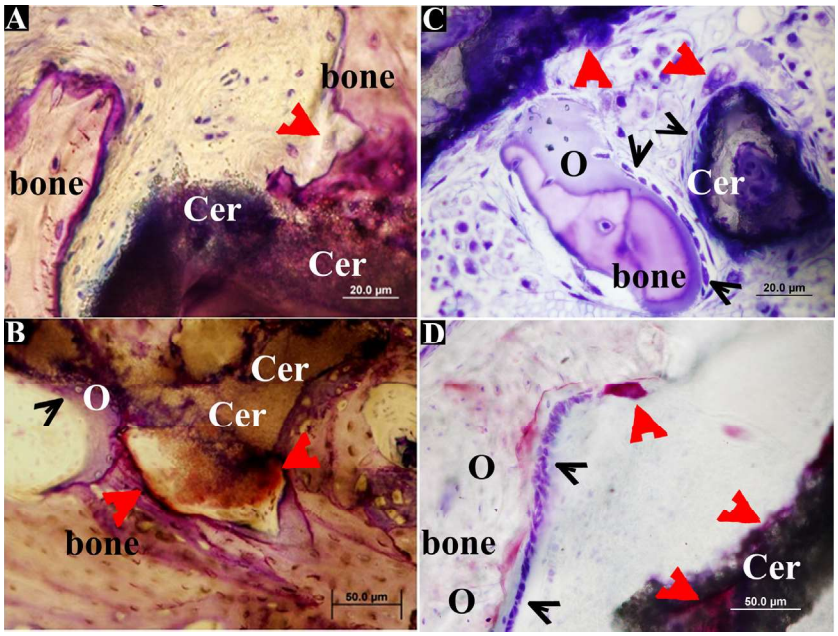

Fig. 7. In vivo histological and enzyme histochemical responses of bone tissue to scaffold implantation. Toluidine blue stained sections (A) and (C) and tartrate resistant acid phosphatase (TRAP) enzyme histochemical stained sections (B) and (D) showed active bone and ceramic remodelling was apparent in the radial defect with Sr–HT–gahnite (C) (D). Both (A, B) TCP/HA and (C, D) Sr–HT–gahnite ceramics showed the presence of bone cells, with osteoblasts (black arrows) laying down osteoid (O) on bone surfaces and TRAP positive osteoclasts (red arrow heads) on both bone and ceramic surfaces. Bone, ceramic (Cer), osteoid (O), osteoblasts (black arrows) and osteoclasts (red arrow heads).

and a similar amount of ceramic was present after 12 weeks for both materials (data not shown).

The sections were assessed qualitatively for bone remodeling activity within the new bone formed in the defects. Osteoblasts were visualized with toluidine blue staining (Fig. 7A and C) and osteoclasts (Fig. 7B and D) were identified by TRAP staining. Numerous osteoblasts and extensive osteoid seams were evident on bone and ceramic surfaces within the defect, and were observed to be more prominent with Sr–HT–gahnite (Fig. 7B and D) than with TCP/HA (Fig. 7A and C). TRAP staining demonstrated the presence of osteoclasts on bone and ceramic surfaces in both TCP/HA and Sr–HT–gahnite filled defects, indicating the potential for osteoclast mediated ceramic removal. Histological measurements thus confirmed the results obtained by radiographic analyses, and also demonstrated marked advantages in Sr–HT–gahnite scaffold structural integrity and the ability to induce new bone formation bridging the entire defect. Sr–HT–gahnite scaffolds not only induced an increased amount of bone formation and improved defect bridging, but also encouraged the formation of new bone with superior architecture and structure, giving clear evidence that the original radial architecture and bone marrow environment were being regenerated. While these results imply structural functionality, it will be important to confirm this through biomechanical studies in future large animal studies experiments. The material showed that at the 12 week time point limited degradation of the implanted scaffold had occurred. It will be important in future studies to evaluate later time points in order to assess the patterns of degradation of Sr–HT–gahnite in vivo.

This study has demonstrated, through microstructural design strategies, the development of a highly promising new ceramic material for the preparation of bioactive scaffolds for bone regeneration. Sr–HT–gahnite scaffolds have been shown to possess superior mechanical properties to currently available materials, as well as significant bioactivity demonstrated by enhanced bone regeneration bridging a critical defect. Thus Sr–HT–gahnite has significant potential for use in surgical procedures where bone regeneration under load-bearing is required.

4. Conclusion

Strong and porous Sr–HT–gahnite scaffolds (porosity: 85%; pore size: 400 μm) with the unique microstructural features showed the capacity to regenerate bone in rabbit radial defects with no adverse effects, i.e. tissue necrosis or inflammation. In vitro, they also significantly enhanced the osteogenic-related gene expression (collagen type I, runx2, bone sialoprotein and osteocalcin) of HOBs compared to TCP/HA scaffolds. The obtained results suggest that Sr–HT–gahnite has potential to address the unmet need for bone substitutes that can be used in load and partial load-bearing sites in orthopedic and trauma applications.

Disclosure statement

No competing financial interests exist.

Acknowledgements

The authors acknowledge funding by the Australian National Health and Medical Research Council and the Rebecca Cooper Foundation and the assistance of the Australian Centre for Microscopy and Microanalysis, University of Sydney. We thank Associate Professor Andrew Minette in the acknowledgment for proof-reading the manuscript.

Appendix A. Figures with essential colour discrimination

Certain figures in this article, particularly Figs. 1–7 are difficult to interpret in black and white. The full colour images can be found in the on-line version, at http://dx.doi.org/10.1016/j.actbio.2013.02.039.

References

[1] Seiler 3rd JG, Johnson J. Iliac crest autogenous bone grafting: donor site complications. J South Orthop Assoc 2000;9:91–7.

[2] Greenwald AS, Boden SD, Goldberg VM, Khan Y, Laurencin CT, Rosier RN. Bone-graft substitutes: facts, fictions, and applications. J Bone Joint Surg Am 2001;83:98–103.
[3] Ikada Y. Challenges in tissue engineering. J R Soc Interface 2006;3:589–601.
[4] Gentleman E, Fredholm YC, Jell G, Lotfibakhshaiesh N, O'Donnell MD, Hill RG, et al. The effects of strontium-substituted bioactive glasses on osteoblasts and osteoclasts in vitro. Biomaterials 2010;31:3949–56.
[5] Fu Q, Saiz E, Rahaman MN, Tomsia AP. Bioactive glass scaffolds for bone tissue engineering: state of the art and future perspectives. Mater Sci Eng C Mater Biol Appl 2011;31:1245–56.
[6] Rezwan K, Chen QZ, Blaker JJ, Boccaccini AR. Biodegradable and bioactive porous polymer/inorganic composite scaffolds for bone tissue engineering. Biomaterials 2006;27:3413–31.
[7] Wagoner Johnson AJ, Herschler BA. A review of the mechanical behavior of CaP and CaP/polymer composites for applications in bone replacement and repair. Acta Biomater 2011;7:16–30.
[8] Legeros RZ, Lin S, Rohanizadeh R, Mijares D, Legeros JP. Biphasic calcium phosphate bioceramics: preparation, properties and applications. J Mater Sci Mater Med 2003;14:201–9.
[9] Hench LL, Polak JM. Third-generation biomedical materials. Science 2002;295:1014–7.
[10] Ritchie RO. The conflicts between strength and toughness. Nat Mater 2011;10:817–22.
[11] Demetriou MD, Launey ME, Garrett G, Schramm JP, Hofmann DC, Johnson WL, et al. A damage-tolerant glass. Nat Mater 2011;10:123–8.
[12] Wondraczek L, Mauro JC, Eckert J, Kühn U, Horbach J, Deubener J, et al. Towards ultrastrong glasses. Adv Mater 2011;23:4578–86.
[13] Li H, Chang J. Preparation and characterization of bioactive and biodegradable Wollastonite/poly(D, L-lactic acid) composite scaffolds. J Mater Sci Mater Med 2004;15:1089–95.
[14] Kim UJ, Park J, Joo Kim H, Wada M, Kaplan DL. Three-dimensional aqueous-derived biomaterial scaffolds from silk fibroin. Biomaterials 2005;26:2775–85.
[15] Roohani-Esfahani SI, Lu ZF, Li JJ, Ellis-Behnke R, Kaplan DL, Zreiqat H. Effect of self-assembled nanofibrous silk/polycaprolactone layer on the osteoconductivity and mechanical properties of biphasic calcium phosphate scaffolds. Acta Biomater 2012;8:302–12.
[16] Ritchie RO. The quest for stronger, tougher materials. Science 2008;320:448.
[17] Munch E, Launey ME, Alsem DH, Saiz E, Tomsia AP, Ritchie RO. Tough, bio-inspired hybrid materials. Science 2008;322:1516–20.
[18] Foulk IJW, Johnson GC, Klein PA, Ritchie RO. On the toughening of brittle materials by grain bridging: promoting intergranular fracture through grain angle, strength, and toughness. J Mech Phys Solids 2008;56:2381–400.
[19] Launey ME, Ritchie RO. On the fracture toughness of advanced materials. Adv Mater 2009;21:2103–10.
[20] Caplan AI. Mesenchymal stem cells: cell-based reconstructive therapy in orthopedics. Tissue Eng 2005;11:1198–211.
[21] Rose FRAJ, Oreffo ROC. Bone tissue engineering: hope vs hype. Biochem Biophys Res Commun 2002;292:1–7.
[22] Salgado AJ, Coutinho OP, Reis RL. Bone tissue engineering: state of the art and future trends. Macromol Biosci 2004;4:743–65.
[23] Hoppe A, Güldal N, Boccaccini A. A review of the biological response to ionic dissolution products from bioactive glasses and glass-ceramics. Biomaterials 2011;32:2757–831.
[24] Lakhkar NJ, Lee IH, Kim HW, Salih V, Wall IB, Knowles JC. Bone formation controlled by biologically relevant inorganic ions: role and controlled delivery from phosphate-based glasses. Adv Drug Deliv Rev 2012.
[25] Roohani-Esfahani SI, Nouri-Khorasani S, Lu Z, Appleyard R, Zreiqat H. The influence hydroxyapatite nanoparticle shape and size on the properties of biphasic calcium phosphate scaffolds coated with hydroxyapatite–PCL composites. Biomaterials 2010;31:5498–509.
[26] Kokubo T, Takadama H. How useful is SBF in predicting in vivo bone bioactivity? Biomaterials 2006;27:2907–15.
[27] Kang Y, Scully A, Young DA, Kim S, Tsao H, Sen M, et al. Enhanced mechanical performance and biological evaluation of a PLGA coated β-TCP composite scaffold for load-bearing applications. Eur Polym J 2011;47:1569–77.
[28] Walker LS, Marotto VR, Rafiee MA, Koratkar N, Corral EL. Toughening in graphene ceramic composites. ACS Nano 2011;5:3182–90.
[29] Wang H, Pallav P, Isgrò G, Feilzer AJ. Fracture toughness comparison of three test methods with four dental porcelains. Dent Mater 2007;23:905–10.
[30] Simpson LA, Hsu TR, Merrett G. Application of the single-edge notched beam to fracture toughness testing of ceramics. J Test Eval 1974;2:503–9.
[31] Gogotsi GA. Fracture toughness of ceramics and ceramic composites. Ceram Int 2003;29:777–84.
[32] Niemeyer P, Szalay K, Luginbühl R, Südkamp NP, Kasten P. Transplantation of human mesenchymal stem cells in a non-autogenous setting for bone regeneration in a rabbit critical-size defect model. Acta Biomater 2010;6:900–8.
[33] Bodde EWH, Spauwen PHM, Mikos AG, Jansen JA. Closing capacity of segmental radius defects in rabbits. J Biomed Mater Res A 2008;85:206–17.
[34] Knabe C, Kraska B, Koch C, Gross U, Zreiqat H, Stiller M. A method for immunohistochemical detection of osteogenic markers in undecalcified bone sections. Biotech Histochem 2006;81:31–9.
[35] Ramay HRR, Zhang M. Biphasic calcium phosphate nanocomposite porous scaffolds for load-bearing bone tissue engineering. Biomaterials 2004;25:5171–80.
[36] Michna S, Wu W, Lewis JA. Concentrated hydroxyapatite inks for direct-write assembly of 3-D periodic scaffolds. Biomaterials 2005;26:5632–9.
[37] Bae CJ, Kim HW, Koh YH, Kim HE. Hydroxyapatite (HA) bone scaffolds with controlled macrochannel pores. J Mater Sci Mater Med 2006;17:517–21.
[38] Santos JD, Reis RL, Monteiro FJ, Knowles JC, Hastings GW. Liquid phase sintering of hydroxyapatite by phosphate and silicate glass additions: structure and properties of the composites. J Mater Sci Mater Med 1995;6:348–52.
[39] Zreiqat H, Ramaswamy Y, Wu C, Paschalidis A, Lu Z, James B, et al. The incorporation of strontium and zinc into a calcium–silicon ceramic for bone tissue engineering. Biomaterials 2010;31:3175–84.
[40] Nilen RWN, Richter PW. The thermal stability of hydroxyapatite in biphasic calcium phosphate ceramics. J Mater Sci Mater Med 2008;19:1693–702.
[41] Koester KJ, Ager Iii JW, Ritchie RO. The true toughness of human cortical bone measured with realistically short cracks. Nat Mater 2008;7:672–7.
[42] Nagels J, Stokdijk M, Rozing PM. Stress shielding and bone resorption in shoulder arthroplasty. J Shoulder Elbow Surg 2003;12:35–9.
[43] Fu Q, Rahaman MN, Sonny Bal B, Brown RF, Day DE. Mechanical and in vitro performance of 13–93 bioactive glass scaffolds prepared by a polymer foam replication technique. Acta Biomater 2008;4:1854–64.
[44] Kim HW, Knowles JC, Kim HE. Hydroxyapatite porous scaffold engineered with biological polymer hybrid coating for antibiotic Vancomycin release. J Mater Sci Mater Med 2005;16:189–95.
[45] Chen QZ, Boccaccini AR. Poly(D, L-lactic acid) coated 45S5 Bioglass®-based scaffolds: processing and characterization. J Biomed Mater Res A 2006;77:445–57.
[46] Fu Q, Saiz E, Tomsia AP. Bioinspired strong and highly porous glass scaffolds. Adv Funct Mater 2011;21:1058–63.
[47] Habibovic P, Kruyt MC, Juhl MV, Clyens S, Martinetti R, Dolcini L, et al. Comparative in vivo study of six hydroxyapatite-based bone graft substitutes. J Orthop Res 2008;26:1363–70.
[48] Chen QZ, Thompson ID, Boccaccini AR. 45S5 Bioglass®-derived glass-ceramic scaffolds for bone tissue engineering. Biomaterials 2006;27:2414–25.
[49] Wu ZY, Hill RG, Yue S, Nightingale D, Lee PD, Jones JR. Melt-derived bioactive glass scaffolds produced by a gel-cast foaming technique. Acta Biomater 2011;7:1807–16.
[50] Jones JR, Ehrenfried LM, Hench LL. Optimising bioactive glass scaffolds for bone tissue engineering. Biomaterials 2006;27:964–73.
[51] Dellinger JG, Wojtowicz AM, Jamison RD. Effects of degradation and porosity on the load bearing properties of model hydroxyapatite bone scaffolds. J Biomed Mater Res A 2006;77:563–71.
[52] Woodard JR, Hilldore AJ, Lan SK, Park CJ, Morgan AW, Eurell JAC, et al. The mechanical properties and osteoconductivity of hydroxyapatite bone scaffolds with multi-scale porosity. Biomaterials 2007;28:45–54.
[53] Jun IK, Song JH, Choi WY, Koh YH, Kim HE, Kim HW. Porous hydroxyapatite scaffolds coated with bioactive apatite-wollastonite glass-ceramics. J Am Ceram Soc 2007;90:2703–8.
[54] Callcut S, Knowles JC. Correlation between structure and compressive strength in a reticulated glass-reinforced hydroxyapatite foam. J Mater Sci Mater Med 2002;13:485–9.
[55] Park YS, Kim KN, Kim KM, Choi SH, Kim CK, Legeros RZ, et al. Feasibility of three-dimensional macroporous scaffold using calcium phosphate glass and polyurethane sponge. J Mater Sci 2006;41:4357–64.
[56] Chen QZ, Efthymiou A, Salih V, Boccaccini AR. Bioglass®-derived glass-ceramic scaffolds: study of cell proliferation and scaffold degradation in vitro. J Biomed Mater Res A 2008;84:1049–60.
[57] Xia W, Chang J. Bioactive glass scaffold with similar structure and mechanical properties of cancellous bone. J Biomed Mater Res B Appl Biomater 2010;95B:449–55.
[58] Zhao J, Lu X, Duan K, Guo LY, Zhou SB, Weng J. Improving mechanical and biological properties of macroporous HA scaffolds through composite coatings. Colloids Surf B Biointerfaces 2009;74:159–66.
[59] Zhao K, Tang YF, Qin YS, Wei JQ. Porous hydroxyapatite ceramics by ice templating: freezing characteristics and mechanical properties. Ceram Int 2011;37:635–9.
[60] Tiainen H, Lyngstadaas SP, Ellingsen JE, Haugen HJ. Ultra-porous titanium oxide scaffold with high compressive strength. J Mater Sci Mater Med 2010;21:2783–92.
[61] Wu C, Ramaswamy Y, Boughton P, Zreiqat H. Improvement of mechanical and biological properties of porous $CaSiO_3$ scaffolds by poly(d, l-lactic acid) modification. Acta Biomater 2008;4:343–53.
[62] Wu C, Zhang Y, Zhu Y, Friis T, Xiao Y. Structure–property relationships of silk-modified mesoporous bioglass scaffolds. Biomaterials 2010;31:3429–38.
[63] Xue W, Bandyopadhyay A, Bose S. Polycaprolactone coated porous tricalcium phosphate scaffolds for controlled release of protein for tissue engineering. J Biomed Mater Res B Appl Biomater 2009;91:831–8.
[64] Cai S, Xu GH, Yu XZ, Zhang WJ, Xiao ZY, Yao KD. Fabrication and biological characteristics of β-tricalcium phosphate porous ceramic scaffolds reinforced with calcium phosphate glass. J Mater Sci Mater Med 2009;20:351–8.
[65] Munar ML, Udoh KI, Ishikawa K, Matsuya S, Nakagawa M. Effects of sintering temperature over 1,300 °C on the physical and compositional properties of porous hydroxyapatite foam. Dent Mater J 2006;25:51–8.